Analysis and visualization of the perturbations imposed on the liquid film by crown sheet collapse or closure

D. Ribeiro[1,*], M. Panão[2], J. Barata[1], A. Silva[1]

1: AEROG, LAETA, Aeronautics and Astronautics Research Center, University of Beira Interior, 6201-001 Covilhã Portugal
2: ADAI, LAETA, Associação para o Desenvolvimento da Aerodinâmica Industrial, University of Coimbra, 3030-788, Coimbra, Portugal
*Corresponding author: daniela.santo.ribeiro@ubi.pt

Keywords: high-speed imaging, bottom perspective, capillary waves, bubble encapsulation.

ABSTRACT

Bubble encapsulation is a phenomenon that results from droplet impact on a liquid film for very specific impact conditions. After splashing, the crown liquid sheet starts to bend inwards, and eventually, the jets at the top of the crown merge and form a perfect empty bubble. This bubble bursts due to the impingement of a secondary droplet that falls in the spherical dome or by reaching its critical thickness. However, bubble encapsulation is seldom reported in the literature. Due to that, this work focuses on understanding better its dynamics and formation mechanisms. By using a bottom perspective of the phenomenon, important information about its dynamics is disclosed. From the bottom shadowgraphs, the capillary waves and the perturbations imposed on the steady liquid film are clearly observed. From previous works, it was confirmed that its occurrence is systematic, so, one of the goals of this study is to realize how the impact conditions influence the phenomenon and if we can establish a criterion for its occurrence. Despite the scarce information about the phenomenon, there are some works about it that are focused on the cavity underneath the bubble. In this study, we observed the cavity and conclude that the cavity shape does not influence the bubble encapsulation phenomenon. Finally, the crown closure time was measured for a specific set of impact conditions and it was analyzed depending on the dimensionless thickness of the liquid film.

1. Introduction

The fundamental hydrodynamic and thermal-induced mechanisms of the single drop impact onto a liquid film have been studied since the time of Worthington (1908). The most complex morphological event occurs when the impact energy is enough to form a liquid crown structure from which instabilities at the bounding rim lead to a secondary atomization process. Several authors identified the splashing phenomenology as prompt splash and crown splash (Yarin et al., 2017; Liang & Mudawar, 2016). However, for specific sets of impact conditions, prompt and crown splash are observed followed by the bending of the liquid crown sheet, and eventually, the jets at

the top can merge and encapsulate a bubble remaining at the top of the liquid film (D. Ribeiro et al., 2019). This bubble can burst by the impingement of secondary droplets that fall on the dome or by reaching a critical thickness due to the drainage of the liquid by the crown sheet walls.

Engel (1966) related the crater of meteorite impacts with the impact of a liquid droplet onto a deep pool and the morphology he presents is similar to the observed for bubble encapsulation even in relatively thin liquid films ($0.2 < h_f/D_0 < 1$) as previously reported (D. Ribeiro et al., 2019). Engel (1966) states the impact energy of the impinging drop exceeds a minimum threshold, which is likely related to splash, and bubble formation attributed to a surface tension effect since the work of Worthington (1908). However, these works focused on the crater dynamics rather than the crown collapsing at the top and encapsulating a small bubble. Pan et al. (2008) and Motzkus et al. (2009) made a qualitative analysis of the bubble encapsulation. Pan et al. (2008) claim that the transition boundary to obtain bubble encapsulation strongly depends on the dimensionless thickness of the liquid film ($\delta = h_f/D_0$). From a different perspective, Motzkus et al. (2009) focused on the mechanisms of bubble bursting that happens due to the hemispherical thickness reduction by the effect of the rising bubble and the drainage of the liquid at the base. Geppert et al. (2016) also observed the phenomenon and confirmed the boundaries for this event for dimensionless film thicknesses lower than the equivalent of a deep pool and within a certain range of impact Weber number ($1000 < \mathrm{We}_D = \rho U_0^2 D_0/\sigma < 1400$). However, none of these authors attempts to describe and explain the hydrodynamics of bubble encapsulation.

As mentioned, for deep pools, the crater dynamics are the main topic of study when the bubble encapsulation event is present (Worthington, 1908; Engel, 1966). However, in this case, bubble entrapment is observed for droplet impact with thin liquid films and the crater does not assume a spherical shape, but rather a half-disc with round edges. Therefore, one of the goals of this study is to understand how the shape of the cavity affects bubble encapsulation using a visualization of the phenomenon from below. Another important question is related to the transition boundary for bubble encapsulation occurrence. What promotes this phenomenon? Can we relate this phenomenon with any existent correlation in the literature?

To answer these questions, the experimental study presented in this work covers a wide range of impact conditions and two different perspectives of the phenomenon to understand how the different parameters influence the formation and occurrence of bubble encapsulation, and how can we predict it.

2. Experimental Techniques

The conventional angle for visualizing drop impact dynamics is 90° from the normal to the impact surface, *i.e.*, from the side. This viewpoint provides relevant information about the phenomena and the possibility to measure and analyze their features, e.g., crown height, diameter and angle, jet height, and number and size of the secondary droplets. However, the lateral images do not allow a complete understanding of the phenomena. On the other hand, examining the results from other

perspectives can give important knowledge. So, in this study, single droplet impacts onto thin liquid films were also captured both from the side and from below. In this way, an experimental facility was designed and built to acquire high-speed imaging of the phenomena.

Figure 1 shows a scheme of the experimental facility. The experimental setup is composed of four main sections: image acquisition system, droplet dispensing system, liquid film container, and the illumination of the impact site. The images were acquired using a high-speed digital camera Photron FASTCAM mini UX50 and a macro lens Tokina AT-X M100 AF PRO D. The camera has 1.3 Megapixel resolution at frame rates up to $2000\ fps$ (frames per second) and up to $160000\ fps$ at reduced image resolution and the lens has a minimum focal length of 0.3 m. The droplet is generated by a medical syringe pump NE-1000 that is connected through medical tubes to a straight-tip stainless steel needle. The pumping rate is 0.5 ml/min to allow the droplet to fall when the gravity force exceeds the surface tension forces. It is possible to vary the impact velocity U_0 by changing the droplet falling height. To hold the liquid film a topless right-angled perspex container was used. The size of the container was calculated to assure that the walls do not interfere with the phenomena. The thickness of the liquid film h_f is defined according to the droplet initial diameter D_0 and dimensionless film thicknesses $\delta = h_f/D_0$ between 0.1 and 1 were tested. Finally, the illumination of the impact site is vital to improve the quality of the images. A set of LED's connected to a power supply was the only light source in the room. Also, a diffusion glass was put between the LED's and the impact site.

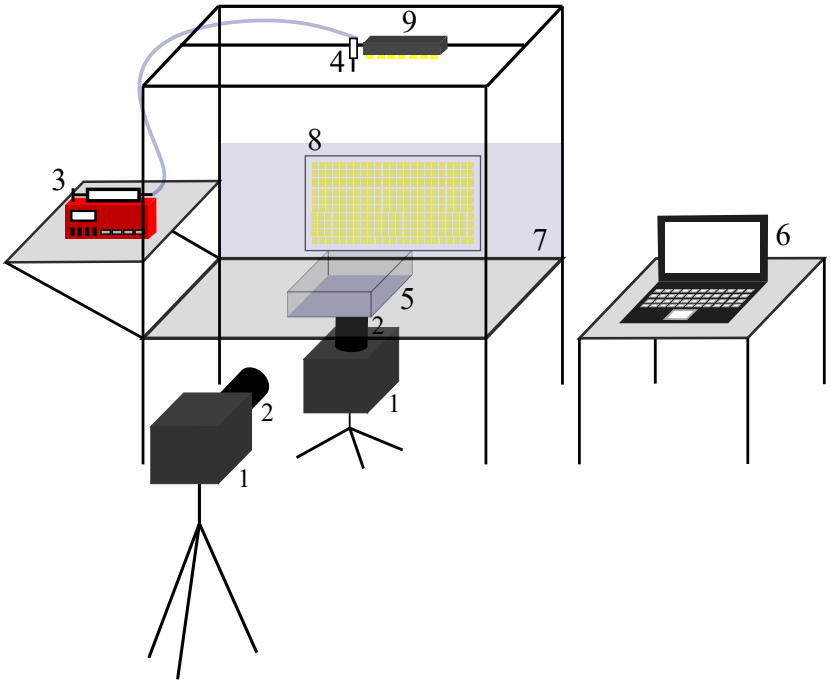

Figure 1. Experimental setup: 1) high-speed digital camera; 2) macro lens; 3) syringe pump; 4) stainless steel needle; 5) liquid film container; 6) computer; 7) diffusion glass; 8 and 9) set of LED's.

As can be seen in Figure 1, the high-speed camera assumed two different positions. For the lateral images, it was placed parallel to the droplet falling plane, but for the bottom images, it was placed

underneath the glass that supports the perspex container. Due to the transparency of the glass, the Perspex, and the fluid of the liquid film, and by placing the camera parallel to the bottom of the container, it is possible to capture shadowgraphs of the impact by using a light source that provides backlighting. Another set of LED's was put next to the dispensing needle providing lighting for the bottom images.

The phenomenon of bubble encapsulation was unexpectedly found in previous works (D. F. Ribeiro et al., 2020; D. Ribeiro et al., 2019, 2020), which were focused on the implementation of biofuels in civil aviation. In this way, fuel mixtures were used in the experiments. At the current times, the legislation allows the use of fuel mixtures with at least 50% in volume of conventional jet fuel (D1655-19a, 2019; D7566-19b, 2019). We decided to keep the same fluids used in D. F. Ribeiro et al. (2020), so, the fluids tested were 100% Jet A-1, a conventional jet fuel, and a mixture that has 75% in volume of Jet A-1 and 25% of NExBTL (Neste Renewable Diesel) a type of HVO (Hydroprocessed Vegetable Oil). The thermophysical properties of these fluids (density ρ, surface tension σ, and dynamic viscosity μ) were measured and are presented in the following table.

Table 1. Fluid thermophysical properties.

Substance	$\rho\ [kg/m^3]$	$\sigma \cdot 10^3\ [N/m]$	$\mu \cdot 10^3\ [Pa \cdot s]$
100% Jet A-1	798.3	25.4	1.12
75% Jet A-1 - 25% NExBTL	794.9	25.5	1.44

The droplet initial diameter D_0 is varied by changing the inner diameter of the dispensing needle, resulting in $2.6 < D_0 < 3.1$ mm. The impact velocity U_0 was varied by changing the droplet falling height, providing impact velocities between 3.9 and 4.8 m/s. The Weber and Reynolds numbers usually characterize the impact. The Weber number We describes the ratio between the inertial and surface tension forces, $We_D = \rho U_0^2 D_0/\sigma$, and the Reynolds number Re is the ratio between the inertial and viscous forces, $Re_D = \rho U_0 D_0/\mu$. In this study, the Weber numbers varied between 1502<We_D<2180 and the Reynolds numbers between 6263<Re_D<8358. Using this experimental facility and the impact conditions described above the phenomenon of bubble encapsulation was observed both from the side and from below and the perturbations imposed on the liquid film by the impact and crown collapse were analyzed.

3. Visualization and Analysis

3.1. Bubble encapsulation phenomenology

Bubble encapsulation is a complex phenomenon resulting from the closure of the crown upper rim in a splash event. The uprising sheet walls reach the maximum height in a relatively short timescale, but the crown base has enough radial momentum to grow into a diameter larger than the crown rim. However, the hydrodynamic reason for keeping the upper rim in a fixed position

can only be the supply of liquid through the vertical crown liquid sheet. As the rim thickens, surface tension forces lead to its collapse forming a bubble above the cavity on the liquid film. Figure 2 shows a sequence of the first stages of impact from a bottom perspective, including illustrations of the lateral perspective. The white in the image implies the light transmitted through a liquid film in a steady state. Once the droplet approaches the film, and after its impact, the curvature reflects light and produces a shadow (Selmke, 2020). After impact, the fingering structures typical of a prompt splash are visible, and the thin white circular line sets the beginning of the kinematic discontinuity forming the uprising crown. The white spot in the first image results from the convergence of light at the top hemisphere of the impinging droplet, which works as a focal lens. This spot enlarges as the droplet mixes with the liquid film, but also the thin line thickens due to the inner curvature of the splashing uprising crown. The third image illustrates the complete immersion of the impinging droplet onto the liquid film forming a disc-shaped crater and the shadow is proportional to the size of the perturbed liquid film forming the base that sustains crown development.

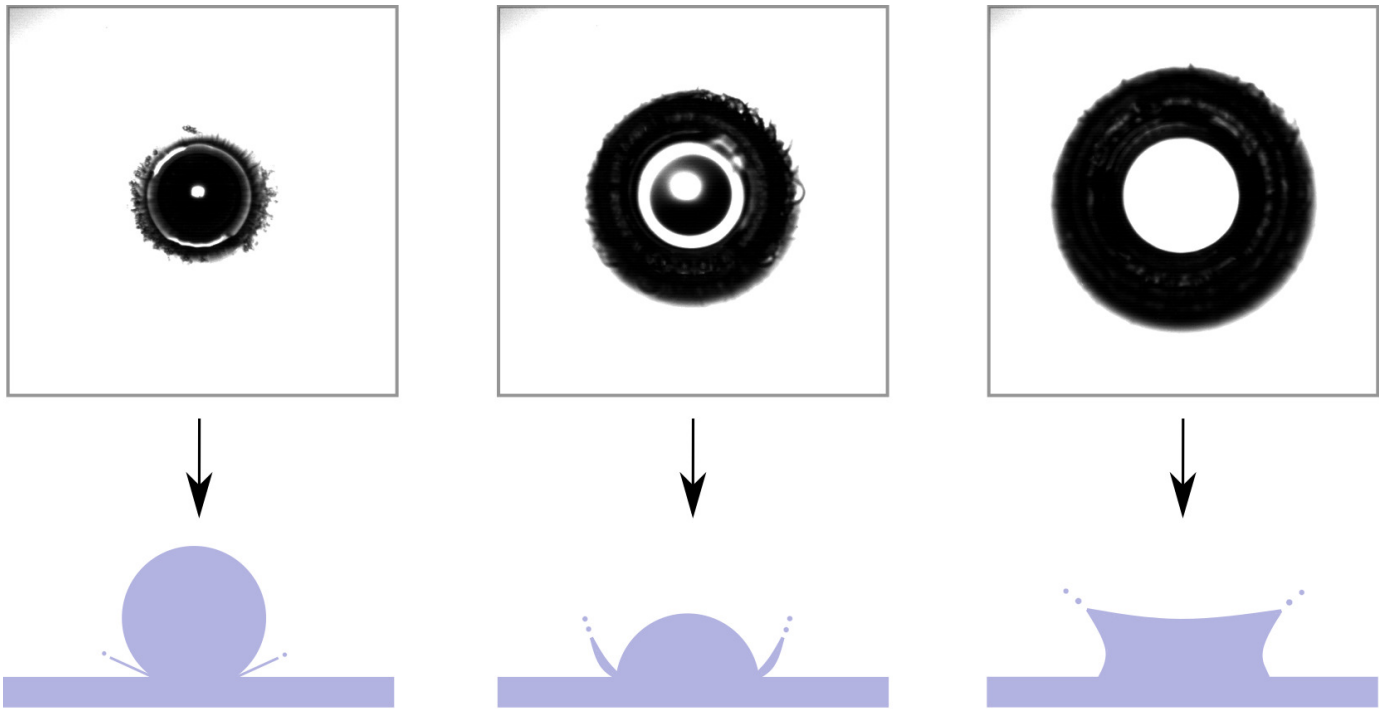

Figure 2. First stages of impact seen from the bottom perspective with schematics of the correspondent images from the lateral perspective.

Crown sheet height keeps increasing and capillary waves start forming at the crown liquid sheet going to the bottom of the crown (Chashechkin, 2019). For high-impact velocities and a combination of fluid thermophysical properties and dimensionless film thickness, the crown walls continue to expand at the base after the crown has reached its maximum height. This implies the timescale of crown formation is shorter than the timescale of the expansion of its base. In these conditions, the crown walls tend to bend inwards, as can be seen in Figure 3 (a). One of the advantages of this type of visualization is the possibility to determine the exact time of crown closure, which is

difficult and inaccurate to define from the side perspective of the impact. Figure 3 (b) shows the exact time when the crown rim merges to form a closed bubble above the liquid film. It is also possible to identify the shapes of capillary waves propagating on the bubble liquid sheet. There are also waves developing from the impact site to the undisturbed liquid film identified by the difference between black, grey, and white areas since the light transverse differently depending on if the curvature of the liquid film is concave or convex.

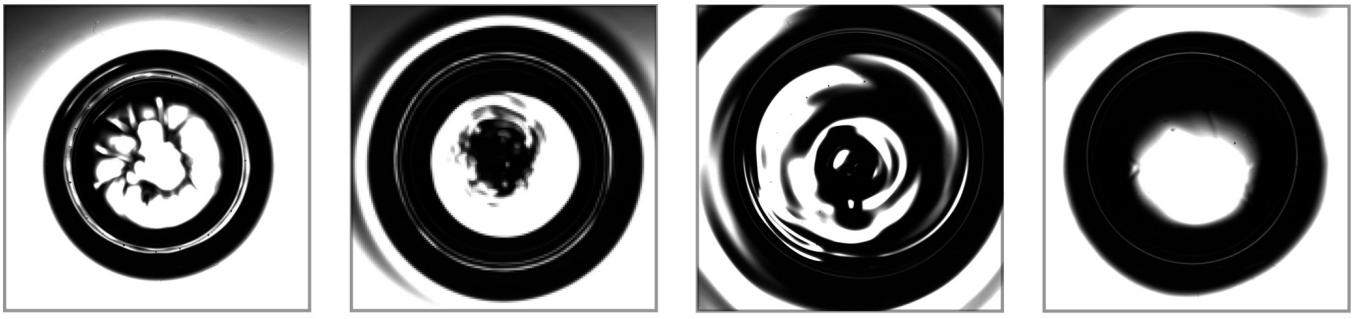

Figure 3. Evolution of the perturbations imposed on the liquid film: (a) crown liquid sheet bending inwards; (b) crown sheet closure; (c) capillary waves propagating down the bubble liquid sheet and to the undisturbed liquid film; (d) steady bubble liquid sheet on a steady liquid film.

Previous studies (Engel, 1966; D. Ribeiro et al., 2020) identified three different bubble encapsulation formation mechanisms. The example shown in Figure 3 is considered Type 1, which involves the formation of a downward jet on the crown closure point. This jet is visible in the center of Figure 3 (c) by a darker circle with a white circle in the middle where the light at the top is fully transmitted to the bottom. The perturbations imposed by the capillary waves, and also the fluid draining from the downward central jet, are visible by the different tones within the dome diameter since the interaction between light and the liquid films curvatures (bubble dome, liquid film) leads to the observed shadowy pattern. Finally, after a long period, these perturbations dissipate and both the horizontal liquid film and the bubble liquid sheet achieve a steady state, Figure 3 (d).

Bubble lifetime further depends on small local instabilities or on the impingement of tiny secondary droplets on the dome. Thus, when the bubble eventually bursts (Fig. 4 (a)), it induces several perturbations in the liquid film. Due to the burst of the bubble liquid sheet, tiny droplets formed with a size scaled by the thin liquid film of the bubble's dome impact the liquid and generate numerous perturbations (Fig. 4 (b)). The capillary waves created by these tiny impacts propagate and interact with each other creating complex patterns, as can be seen in Fig. 4 (c) and (d). From this bottom perspective, it is possible to observe the capillary waves' behavior and understand their evolution within and outside the area delimited by the pre-existing bubble dome. Another important finding of this study is the influence of the liquid film area. If the liquid film area is too small the capillary waves will impact the walls, and bounce back toward the impact site affecting the rest of the phenomenon. This can be of value for numerical simulations.

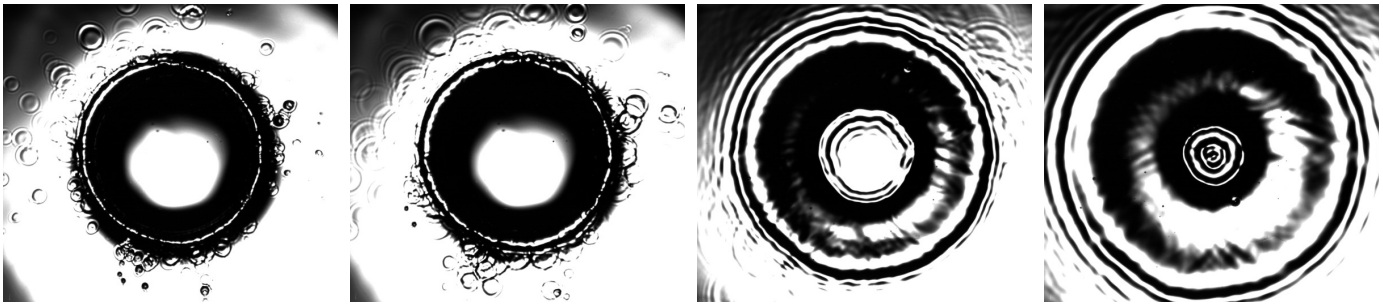

(a) (b) (c) (d)

Figure 4. Bubble bursting and propagation of capillary waves.

3.2. Thresholds of bubble encapsulation

For certain sets of impact conditions, the bubble encapsulation phenomena occur 100% meaning these have a probability of occurrence equal to unity, $p = 1$. However, there are also cases where $p < 1$. For the range of impact conditions studied, Fig. 5 shows the probability of occurring bubble encapsulation depending on the dimensionless thickness of the liquid film δ and considering a minimum sample of 10 events. The white bars represent a bubble encapsulation occurrence of 100%, $p = 1$, the red bars with 80%, $p = 0.8$, and the blue bars between 50% and 80%, $0.5 \leq p < 0.8$. The δ range considered varies between 0.4 and 1.0. Events of bubble encapsulation were observed for $\delta = 0.2$ and $\delta = 0.3$ but with $p < 0.5$, and were not considered here. Thus, there is a minimum dimensionless film thickness required to produce this phenomenon. For $0.4 \leq \delta \leq 1.0$, the 100% occurrence of bubble encapsulation is guaranteed but only for certain sets of impact conditions. By using different impact energies with a constant dimensionless thickness of the liquid film δ, the event can be observed but with a lower probability. In the experiments with $\delta = 0.6$ and $\delta = 1.0$, the several impact energy conditions tested changed because of the impact velocity U_0, and the probability to observe bubble encapsulation varied between 100% and 50%. For the dimensionless thicknesses of 0.5, 0.7, and 0.9 only one set of impact conditions was tested. Bubble encapsulation has been observed for this set of conditions for other dimensionless thicknesses, so, it was tested for these specific thicknesses to assure that the occurrence probability was kept while changing the thickness of the liquid film.

Bubble encapsulation is the second outcome after a splashing event triggered by a kinematic discontinuity at the boundary of the impinging droplet and the liquid film. Therefore, bubble encapsulation depends on a combination of viscous, inertial, and surface tension forces. First, we decided to compare these results with correlations available in the literature for the splashing threshold. According to D. F. Ribeiro et al. (2020), the majority of the empirical correlations that define the transition between spreading and splashing K_c are in the form of:

$$Re_D^{\alpha} We_D^{0.8} = K_c \tag{1}$$

After analyzing different empirical correlations, D. Ribeiro et al. (2019) reported that the univer-

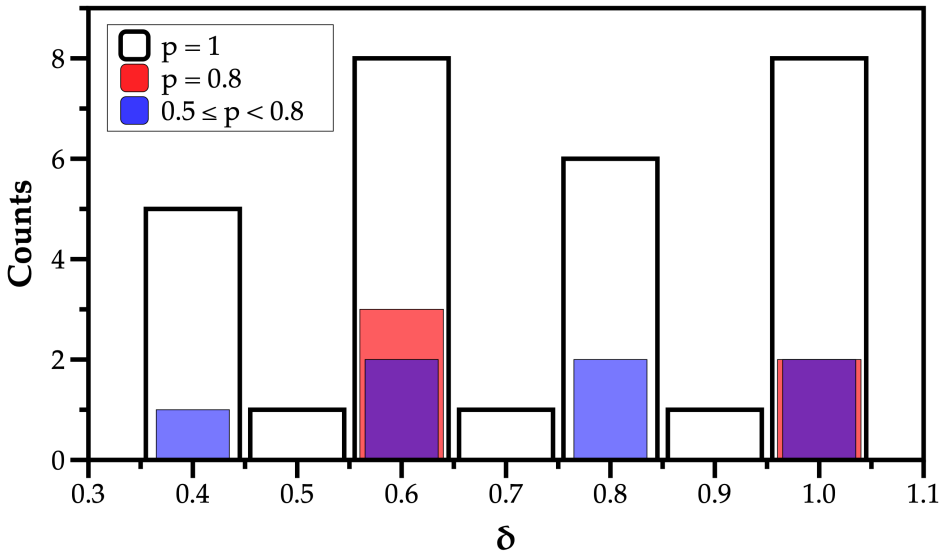

Figure 5. Bubble encapsulation events and their respective probability of occurrence p depending on the dimensionless thickness of the liquid film δ.

sality of the criterion proposed by Vander Wal et al. (2006) provides a better agreement with their experimental data both within and without its validation domain. The Vander Wal et al. (2006) correlation is defined as:

$$Re_D^{0.272} We_D^{0.8} = 756.7 \tag{2}$$

However, considering the Ohnesorge number relates all three forces involved in the morphology of bubble encapsulation, rearranging the correlation to include the Ohnesorge number, $Oh_D = \sqrt{We_D}/Re_D$, which relates the viscous forces to the inertial and surface tension forces, the general form of Eq. (1) becomes

$$Re_D Oh_D^a = K_c \tag{3}$$

Considering this, the Vander Wal et al. (2006) transition boundary becomes:

$$Re_D Oh_D^{0.8547} = 34.5 \tag{4}$$

Figure 6 compares the Vander Wal et al. (2006) correlation with our data (Re_D and Oh_D), considering the events of bubble encapsulation with different probabilities of occurrence. The black solid line represents the Vander Wal et al. (2006) criterion from the transition between spreading and splashing after the droplet impact onto a liquid film, which does not depend on the dimensionless thickness of the liquid film. The white symbols describe the conditions where bubble encapsulation occurred for $p = 1$, the red middle-size ones for $p = 0.8$, and the blue smaller-size ones for $0.5 \leq p < 0.8$. The experimental results are within a region defined by a bottom (red line) and

top (blue line) boundaries with the corresponding a and K_c values. Considering the Vander Wal et al. (2006) criterion, the bottom boundary was defined by only changing the exponent a value. Resulting in a transition parallel to the one defined by them on a logarithmic scale. Regarding the top boundary, the transition was identified but does not follow the same trend, changing the values of a and K_c as $\mathrm{Re}_D\mathrm{Oh}_D^{2.2} = 0.1$.

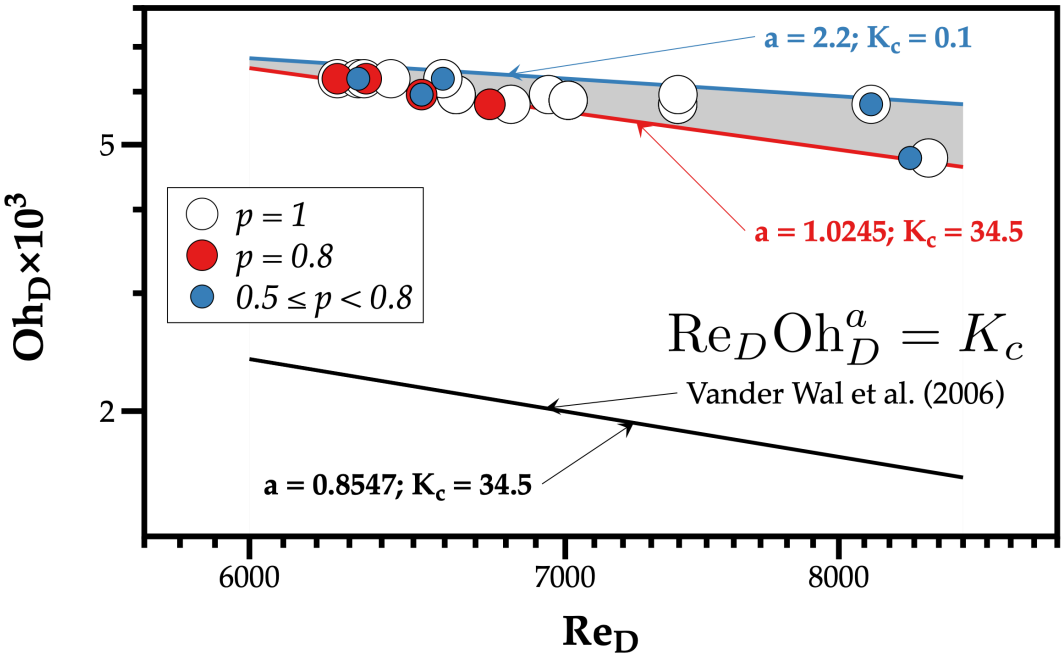

Figure 6. Bubble encapsulation events compared with the spreading/splashing transition boundary of Vander Wal et al. (2006).

However, the aforementioned analisys based on the Vander Wal et al. (2006) correlation does not take into account the influence of the dimensionless liquid film thickness δ. Considering several studies reported in the literature (Josserand et al., 2016; Aljedaani et al., 2018; Lu et al., 2020), the material of the crown sheet formed after the impact of droplets onto liquid films is mainly composed of liquid from the film, instead of the main droplet. This fact is relevant in our study. Therefore, instead of considering the Ohnesorge characteristic length as the initial drop diameter (Oh_D), we modified the Vander Wal et al. (2006) transition boundary to consider the Ohnesorge number characteristic length scale based on the liquid film thickness h_f, Oh_f.

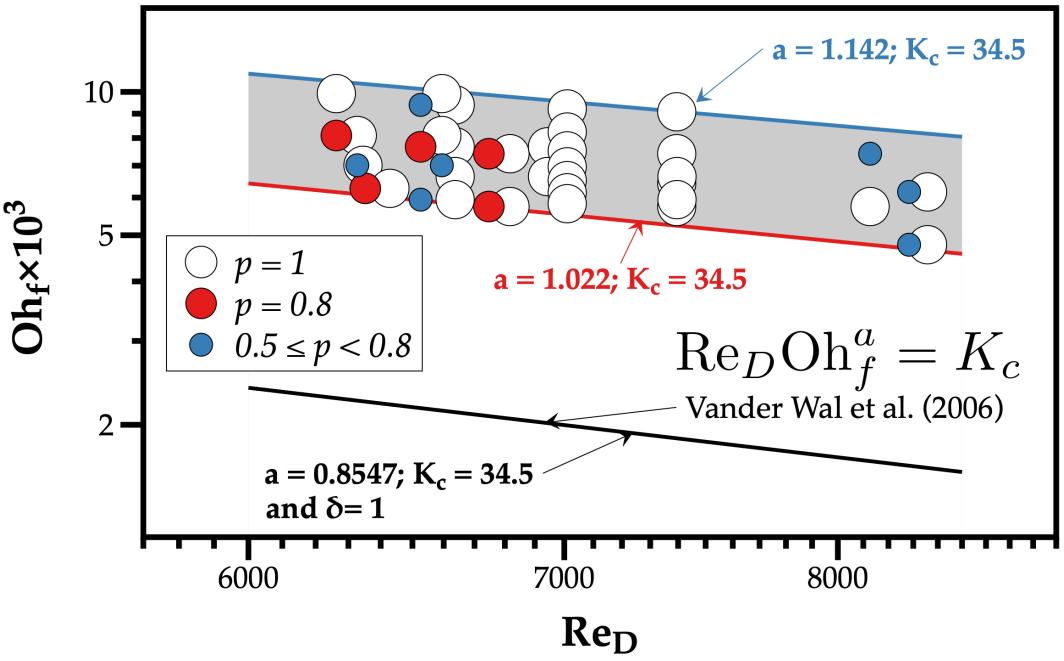

Figure 7. Bubble encapsulation events compared with the spreading/splashing transition boundary of Vander Wal et al. (2006) using the thickness of the liquid film h_f as the characteristic length scale in the calculation of the Ohnesorge number, Oh_f.

Figure 7 shows a similar approach to Fig. 6 but indicates a clearer region where one can expect the occurrence of bubble encapsulation Thus, there are two limiting boundaries based on the Vander Wal et al. (2006) correlation setting the beginning of impact conditions that lead to bubble encapsulation (red line in Fig. 7) and when this phenomenon ceases to occur (blue line), meaning bubble encapsulation occurs for $1.022 < a < 1.142$. Since K_c value is constant for all equations, $K_c = 34.5$, one can develop a criterion for the onset of bubble encapsulation as

$$a = \ln(34.5/\mathrm{Re}_D)/\ln(\mathrm{Oh}_f),\ \forall a \in [1.022, 1.142] \tag{5}$$

valid for $\mathrm{Re}_D \in [6263; 8358]$ and $\mathrm{Oh}_f \times 10^3 \in [4.776; 9.918]$.

The cavity underneath the bubble has been a topic of study (Worthington, 1908; Engel, 1966; Pan et al., 2008). However, this study proves that bubble encapsulation is not promoted by the formation of a hemispherical crater. The shape of the crater is determined by the thickness of the liquid film. For deep pools, the cavity formed is usually hemispherical. In this case, the cavity touches the bottom of the container, as can be seen in Fig. 8. At first, when the crown sheet is still growing in height, the cavity assumes a cylindrical shape and touches the bottom of the container. As the crown sheet wall bends and closes the cavity becomes round at the sides, but still touching the bottom. This shows that it is not necessary to have a fully developed cavity or a specific cavity shape to allow the formation of bubble encapsulation.

One of the benefits of the bottom images concerns the accurate determination of the crown closure time $t_{closure}$. From this perspective, it is clear when the jets at the top close to form the spherical

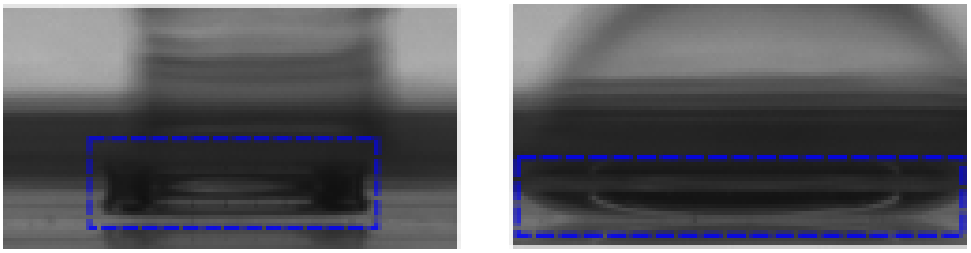

Figure 8. Cavity shape during crown sheet development (left) and during bubble encapsulation (right).

dome. The impact conditions were kept constant at $We = 1667$ and $Re = 7010$, and only the dimensionless film thickness was varied between $0.2 < \delta < 1.0$. Figure 9 shows the crown closure time depending on the dimensionless thickness of the liquid film. The crown closure time slowly increases until $\delta = 0.5$ and then significantly decreases for $\delta = 0.6$. Thenceforth, gently decreases until $\delta = 1.0$. So, we can conclude that thicker thicknesses promote the quick closure of the crown. However, a question arises: Why the abrupt change in crown closure time between $\delta = 0.5$ and $\delta = 0.6$?

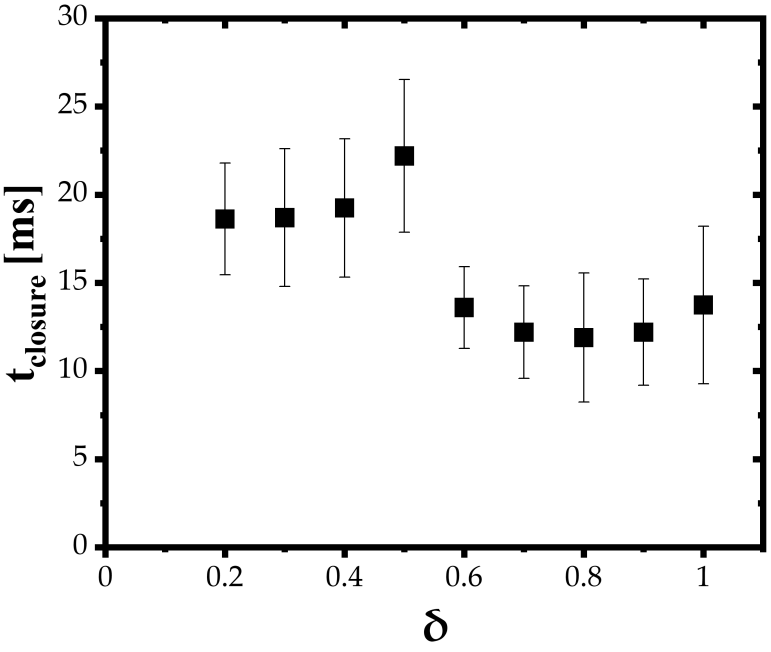

Figure 9. Crown closure time depending on the dimensionless thickness of the liquid film.

4. Conclusions

This study is focused on bubble encapsulation, a phenomenon that happens due to a single droplet impact on a liquid film for specific impact conditions. A wide parameter space was experimentally tested using two different perspectives of the phenomenon (lateral and bottom) to achieve several

sets of impact conditions where bubble encapsulation was observed with 100% occurrence. However, there are also cases where the phenomenon is observed but with a lower probability. In an attempt to predict the occurrence of bubble encapsulation and relate it with any existing correlation in the literature, the experimental data was compared with the spreading/splashing transition criterion proposed by Vander Wal et al. (2006). The equation was rearranged to include the Ohnesorge number calculated using the thickness of the liquid film as the characteristic length scale. In this way, it was possible to define a region where bubble encapsulation is observed. This region is limited by a bottom and a top boundary which derive from the Vander Wal et al. (2006) correlation. The cavity created by these impacts was observed and its shape does not influence the phenomenon since it touches the bottom of the container due to the small thickness of the liquid film.

In the literature, the phenomenon has been photographed from a lateral perspective. However, with a bottom perspective, it is possible to observe important characteristics and improve the knowledge about bubble encapsulation. Using this perspective, the capillary waves and perturbations were observed and the crown closure time was measured. Crown closure time depends on the dimensionless film thickness and shows an abrupt decrease between $\delta = 0.5$ and $\delta = 0.6$.

Acknowledgements

The authors would like to acknowledge the support of Fundação para a Ciência e a Tecnologia (FCT) through the Ph.D. scholarship SFRH/BD/140009/2018 and the project UIDB/50022/2020.

Nomenclature

D_0	Droplet initial diameter [m]
h_f	Liquid film thickness [m]
K_c	Criterion between spread and splash [-]
Re_D	Droplet Reynolds number [-]
$t_{closure}$	crown closure time [s]
U_0	Impact velocity [m/s]
We_D	Droplet Weber number [-]
δ	Dimensionless liquid film thickness [-]
μ	Dynamic viscosity [Pa·s]
ρ	Density [kg/m^3]
σ	Surface tension [N/m]

References

Aljedaani, A. B., Wang, C., Jetly, A., & Thoroddsen, S. T. (2018). Experiments on the breakup of drop-impact crowns by marangoni holes. *Journal of Fluid Mechanics*, *844*, 162–186.

Chashechkin, Y. D. (2019). Visualization of the fine perturbation structure of a liquid surface by flows induced by a drop impact. *Fluid Dynamics*, *54*(7), 919–926.

D1655-19a, A. (2019). *Astm d1655-19a, standard specification for aviation turbine fuels* (Tech. Rep.). ASTM International.

D7566-19b, A. (2019). *Astm d7566-19b, standard specification for aviation turbine fuel containing synthesized hydrocarbons* (Tech. Rep.). ASTM International.

Engel, O. G. (1966). Crater depth in fluid impacts. *Journal of Applied Physics*, *37*(4), 1798–1808.

Geppert, A., Chatzianagnostou, D., Meister, C., Gomaa, H., Lamanna, G., & Weigand, B. (2016). Classification of impact morphology and splashing/deposition limit for n-hexadecane. *Atomization and Sprays*, *26*(10).

Josserand, C., Ray, P., & Zaleski, S. (2016). Droplet impact on a thin liquid film: anatomy of the splash. *Journal of Fluid Mechanics*, *802*, 775–805.

Liang, G., & Mudawar, I. (2016). Review of mass and momentum interactions during drop impact on a liquid film. *International Journal of Heat and Mass Transfer*, *101*, 577–599.

Lu, L., Pei, Y., Qin, J., Peng, Z., Wang, Y., & Zhu, Q. (2020). Impingement behaviour of single ethanol droplet on a liquid film of glycerol solution. *Fuel*, *276*, 117820.

Motzkus, C., Gensdarmes, F., & Géhin, E. (2009). Parameter study of microdroplet formation by impact of millimetre-size droplets onto a liquid film. *Journal of aerosol science*, *40*(8), 680–692.

Pan, K.-L., Cheng, K.-R., Chou, P.-C., & Wang, C.-H. (2008). Collision dynamics of high-speed droplets upon layers of variable thickness. *Experiments in fluids*, *45*(3), 435–446.

Ribeiro, D., Panão, M., Silva, A., & Barata, J. M. (2019). Insights on bubbling formation after drop impact on thin liquid films. In *Ilass 2019-29th european conference on liquid atomization and spray systems.*

Ribeiro, D., Panao, M. O., Barata, J. M., & Silva, A. R. (2020). Morphology of bubble formation on droplet impact upon thin liquid layers. In *AIAA Scitech 2020 Forum* (p. 1577).

Ribeiro, D. F., Silva, A. R., & Panão, M. R. (2020). Insights into single droplet impact models upon liquid films using alternative fuels for aero-engines. *Applied Sciences*, *10*(19), 6698.

Selmke, M. (2020). Bubble optics. *Applied Optics*, *59*(1), 45–58.

Vander Wal, R. L., Berger, G. M., & Mozes, S. D. (2006). The splash/non-splash boundary upon a dry surface and thin fluid film. *Experiments in fluids*, *40*(1), 53–59.

Worthington, A. M. (1908). *A study of splashes*. Longmans, Green, and Company.

Yarin, A. L., Roisman, I. V., & Tropea, C. (2017). *Collision phenomena in liquids and solids*. Cambridge University Press.